Texture and Grain Evolutions in a 2195 Friction Stir Weld

R.W. Fonda, J.F. Bingert[†], and K.J. Colligan[‡]
US Naval Research Laboratory, Washington, DC
[†]Los Alamos National Laboratory, Los Alamos, NM
[‡]Concurrent Technologies Corporation, Johnstown, PA

Abstract

Variations in microstructure, crystallographic texture, and grain distributions were determined in a conventional transverse cross section of the deposited weld and in a plan-view cross section around the embedded welding tool in an Al 2195 friction stir weld that had been prepared to preserve a static representation of the dynamic deformation field surrounding the tool. These results reveal important new details about the development of grain structure and crystallographic texture around the FSW tool that cannot be determined from observations on the transverse cross section alone.

1. Introduction

Friction stir welding (FSW) was developed in 1991 [1] and has rapidly become an important process for joining aluminum alloys. However, despite the widespread growth of FSW as a commercial joining process, the development and evolution of the microstructure to produce the final weld are still not well understood.

FSW is a solid-state joining technique in which a rotating tool is plunged into the material and traversed along the joint line. The rotating tool heats the surrounding material enough to allow plastic deformation (stirring) which intermixes the two sides of the joint line together and form the weld. This produces a fine-grained region called the weld nugget in the center of the weld. The fine grain size of this region is normally considered to be the result of dynamic recrystallization. A region called the thermo-mechanically affected zone (TMAZ) surrounds the weld nugget and contains material that was mechanically deformed and modified by the heat of welding. Outside of the TMAZ is the heat affected zone (HAZ), where the material was influenced by the heat of welding but was not mechanically deformed. This is similar to the HAZ observed in conventional welds.

During the FSW process, the rotating tool induces a complex plastic deformation in the surrounding material that varies as a function of the welding tool geometry. Threading on the tool can cause a downward component to the material flow, inducing either a counterflow extrusion towards the top of the weld [2] or an essentially circumferential flow around the pin. This material flow has been examined experimentally by tracking the flow of embedded tracer materials through sectioning, standard radiography, or X-ray tomography [2-10] and by examining the material distribution after welding dissimilar materials [11,7]. Of particular relevance to the present work are the studies utilizing stop-action techniques. Studies by Colligan [2] and later by Dickerson et al [9] have employed a method of retracting the rotating welding tool at the end of a weld at a rate which caused the welding tool to unscrew from the keyhole, thus leaving material that was in the threads during the welding process intact. However, this approach does not work in cases where the pin has reentrant features such as flats. Such a tool requires an approach similar to that followed by McClure et al [8] and London et al [10], in which power is suddenly removed from the welding machine to stop the pin's rotation and leave the tool embedded in the workpiece. This approach uses the

resistance of the workpiece material to quickly stop the tool's rotation and thereby preserve the complex deformation field that existed around the welding tool during friction stir welding. This is the approach used in the present study.

There have been a number of previous studies characterizing the grain structures and textures produced during friction stir welding [12-20]. However, few of these studies systematically examine the variations in grain structure or texture across the weld. In addition, all of these studies are focused on the deposited weld and therefore do not reveal the initial development and evolution of those grain structures and textures which occur ahead of the welding tool. The current paper examines not only the microstructural and texture characteristics of the deposited weld, but will also examine the development and evolution of grain structure and crystallographic texture around the welding tool itself.

2. Experimental Procedure

The weld examined in this study was prepared by friction stir welding a single 25 mm-thick plate of the aluminum-lithium alloy 2195 in a bead-on-plate configuration. This plate was prepared in an underaged temper developed by Concurrent Technologies Corporation for ballistic performance. The friction stir welding was performed under load control at a rotational speed of 180 revolutions/minute and a translational speed of 1.7 mm/s (4 inches/minute). The tool consisted of a flat, scrolled shoulder and a truncated cone-shaped pin with threads and three flats.

Transverse cross sections were removed from the center of the deposited weld and polished using a Struers Rotopol-31/Rotoforce-4 automatic polisher down to a final polish with a 0.05 μm silica suspension. Optical microscopy was performed on a polished section etched with Keller's reagent and a 50% nitric acid solution in water. A LECO Automated Microhardness Hardness tester was used to acquire microhardness measurements across the facing polished cross section with a load of 300 g and at a vertical and horizontal spacing of 0.4 mm. This section was subsequently etched for direct comparison to the optical microscopy specimen. An additional transverse cross section was electropolished for 30 s in a solution of 30% nitric acid in methanol at approximately –20 °C with an applied potential of 15 V for obtaining electron backscattered diffraction (EBSD) scans in a Leo 1550 SEM equipped with TSL OIM hardware and software.

Specimens for transmission electron microscopy (TEM) of the different weld regions were prepared by electro-discharge machining out 3 mm diameter cylinders from local regions of interest along the weld direction. Slices from these cylinders were mechanically thinned, then polished in a twin-jet electropolisher with a solution of 30% nitric acid in methanol at –20 ºC and 12 V (~50 mA). TEM of these samples was performed on a CM30 TEM.

In order to preserve the dynamic deformation field surrounding the friction stir welding tool, the emergency stop was engaged during welding and the workpiece was immediately quenched with water. The tool rotation stopped within about 0.1 s, or 1/6 of a tool rotation, and the plate cooled to less than 100 °C within a minute. The tool shoulder was removed from the pin but the pin, which could not be retracted from the plate because of its complex geometry, was left embedded in the plate. The end of the weld containing the embedded tool was sectioned by electro-discharge machining at a depth of 10.4 mm (0.41") from the top surface. The upper specimen was prepared in a manner similar to the transverse cross section discussed above. The lower specimen was sectioned into quarters to enable extraction of the MP 159 pin material. The quartered sections were ground and polished, and then

electropolished for 30 s in a solution of 30% nitric acid in methanol at approximately –20 °C with an applied potential of 15 V to enable EBSD analyses of the plan view surface.

3.0 Results and Discussion

3.1 Transverse Cross Section Microstructure

The transverse cross section of this friction stir weld (Figure 1a) exhibits features typical of many friction stir welds. The refined grain structure of the weld nugget region is clearly visible, with a sharply defined nugget boundary on the advancing side but a more gradual change from the deformed grains into the nugget on the retreating side. The weld nugget also exhibits banding that appears similar to the "onion ring" structure often observed in friction stir welds. The grains in the TMAZ, which appear dark in this figure, appear to be systematically deflected upwards on the retreating side and downward on the advancing side.

The microhardness across this transverse cross section (Figure 1b) decreases across the HAZ to a minimum microhardness at the HAZ/TMAZ boundary, after which it increases towards the weld nugget, similar to the observations in other age-hardened aluminum alloys. This has been proposed [e.g.,19,21-24] to be due to aging effects induced by the heat of welding in the HAZ. Strengthening precipitates are coarsened throughout the HAZ, then begin to dissolve from the higher heats experienced in the TMAZ, allowing the formation of fine precipitates during cooling. At the TMAZ/weld nugget boundary, the microhardness characteristics of this weld deviate from those of most other friction stir welds. Whereas the microhardness typically continues to increase inside the weld nugget, or at least maintain a relatively constant value similar to that observed in the TMAZ, the microhardness of this weld exhibits a sharp decrease of 10 to 15 VHN crossing from the TMAZ to the weld nugget (Figure 1c).

To determine the microstructural causes of these microhardness variations, transmission electron microscopy (TEM) and electron diffraction was performed on samples from the various weld zones. Within the HAZ (just outside of the band of minimum microhardness), the heat of welding caused the T_1 and θ' strengthening precipitates to significantly coarsen, increasing the average size of the precipitates and sharpening their diffraction reflections as seen in Figures 2a and 2d. This precipitate coarsening is responsible for the observed decrease in microhardness of this region relative to that of the unaffected base plate.

A different precipitate distribution is observed to gradually replace the T_1 and θ' precipitates across the TMAZ, until no more T_1 and θ' precipitates remain in the peak hardness region just outside the weld nugget (Figures 2b and 2e). These precipitates adjacent to the weld nugget have the spherical shape and diffraction reflections of the Al_3Li phase, δ'. Additionally, there are prominent streaks between the matrix reflections in the electron diffraction pattern which indicate the formation of fine Guinier-Preston (G-P) zones. The increasing numbers of these fine G-P zones and δ' precipitates from the HAZ side of the TMAZ towards the weld nugget account for the corresponding increase in microhardness across the TMAZ. The formation of these precipitates also indicates that the T_1 and θ' precipitates present before welding experienced varying degrees of dissolution in the TMAZ, ranging from partial dissolution near the HAZ to complete dissolution near the weld nugget, during the welding process. This identifies the location of the band of minimum microhardness to be where the precipitates had experienced a maximum of coarsening without any dissolution. Since this band is located at the HAZ/TMAZ boundary, this indicates that even the significantly coarsened precipitates in the HAZ may be sufficient to inhibit the deformation associated with friction stir welding, Similarly, dissolution of these precipitates at high temperatures (before cooling induces precipitation of the G-P zones and

δ' precipitates) may make the material in the TMAZ susceptible to the high-temperature deformation. This characteristic was also observed previously in 2519 friction stir welds [24].

The microstructure undergoes an abrupt change between the TMAZ and the weld nugget. In addition to the refined grain size within the nugget, the precipitates that predominate in the weld nugget have a rod-shaped morphology (Figure 2f) with many orientation variants, producing many additional diffraction reflections (Figure 2c). These precipitates are often observed to be associated with spherical precipitates (see Figure 2f). The rod-shaped precipitates were identified by electron diffraction (Figure 3) as T_B, which have an Al_7Cu_4Li composition and a CaF_2 structure. It is known that T_B often nucleates at β' (Al_3Zr) precipitates, which have the same spherical shape and diffraction appearance as the δ' precipitates present in the TMAZ. Chemical analysis to identify these spherical precipitates has not yet been performed. The electron diffraction patterns again exhibit streaking between the matrix reflections, indicating the presence of G-P zones in this region as well. However, the presence of significant T_B precipitation would reduce the solute available for G-P zone formation and likely result in a lower number of G-P zones, which provide more potent strengthening compared to the coarser precipitates, accounting for the lower microhardness across this region.

3.2 Transverse Cross Section Texture and Grain Evolution

Electron backscattered diffraction (EBSD) was used to observe details of the grain and texture variations on the advancing side of the weld. A montage of EBSD crystal direction maps is shown in Figure 4, in which the color scale is referenced to the standard stereographic triangle for cubic symmetry. An interesting feature of this image is the apparent selective grain coarsening that has occurred near the weld nugget; this phenomenon is observed on both the advancing and retreating sides of the weld. This may be due to thermally activated grain growth processes operating without enough concomitant plastic work to refine the structure in this narrow thermomechanical regime. The grains also typically experience a change in orientation, indicated by the color change with respect to the welding (viewing) direction in Figure 4, as they approach the weld nugget.

The boundary between the TMAZ and the refined grains of the weld nugget is well-defined on the advancing side. However, thin bands of refined grains can be observed extending more than 0.25 mm into the TMAZ. Those grains tend to be close to <001>||welding direction (WD) in orientation (red-orange in color) and appear to develop from single grains in the TMAZ. These refined grains are relatively constant in size and similar to the size of the developing subgrains, although they exhibit a range of orientations. Thus, this grain refinement in the TMAZ may be due to isolated grains with a more susceptible orientation undergoing dynamic recrystallization or deformation-induced subdivision. The grains which do not become refined often have <110>||WD (green color) by the weld nugget. These orientations are expected to be more stable to the applied deformation field, as the shear direction is aligned with the fcc slip direction, <110>.

The variation in grain boundary misorientation across this region is shown in Figure 5. Although the density of low (2-5°) and medium (5-15°) angle boundaries remains relatively constant from the TMAZ into the weld nugget, the large increase in high (>15°) angle grain boundaries in the weld nugget produces the variations observed in this figure. This plot shows a variation in the number of high angle grain boundaries extending more than 200 μm on either side of the weld nugget boundary, reflecting the bands of refined grains which extend into the TMAZ as well as the coarser grains present just inside the weld nugget boundary.

EBSD scans of the weld nugget boundary on the retreating side (Figure 6a) reveal a much more gradual transition between the TMAZ and the weld nugget than was observed on the advancing side. Otherwise, the retreating side of the weld exhibits many of the same characteristics that were observed on the advancing side. Many unrefined grains adjacent to the weld nugget are coarser than those found in the base material. In addition, the orientations of the grains again evolve with respect to the WD (viewing direction), while remaining nearly constant with respect to the weld normal direction (ND), indicating an in-plane rotation about the ND. The evolution of the internal orientations of the three largest grains in Figure 6a are shown in Figure 6b. In each case, the trend is a rotation of <110> toward WD (towards the center of the pole figure) as the grain approaches the weld nugget. This direction is along the shear direction of the rotating tool, indicating that this texture evolution primarily results from a simple-shear deformation field surrounding the tool.

3.3 Plan View Cross Section Microstructure

Mechanisms concerning the development of grain structure and crystallographic texture are difficult (at best) to infer from the information contained in a transverse cross section of the deposited weld. Thus, a stop-action weld was produced in an effort to preserve a "frozen" representation of the dynamic deformation field and the grain refinement process occurring adjacent to the welding tool. The welding process was stopped and the workpiece was immediately quenched with cold water. Because the tool used for this friction stir weld had three flats, it could not be removed without disturbing the adjacent material so the tool was left embedded in the plate. Examinations were performed at a depth of 10.4 mm (0.41") below the top surface, as shown in Figure 7, to reduce the effects of the shoulder while maintaining a large width to the TMAZ and HAZ regions.

An optical image of the plan view cross section of the end of this stop-action weld, including the embedded pin tool, is shown in Figure 8. The three flats on the sides of the tool are evident, as is the deformation surrounding the tool. The deformation is confined to the near vicinity of the tool, particularly on the advancing side. The grains in the TMAZ appear to be consistently deformed in the direction of tool rotation, i.e., in the welding direction on the advancing side and opposite the welding direction on the retreating side, consistent with deformation induced by simple shear. This shearing of the TMAZ grains around the tool is consistent with the in-plane rotations observed on both sides of the weld in the transverse cross section TMAZ (see section 3.2). The vertical deflections of the TMAZ grains observed in the transverse cross section indicate that there is also a vertical component to the TMAZ deformation, although the rotational shear appears to predominate. Material flow studies by other researchers [2-11] have found direct evidence of vertical mixing, although the amount of vertical mixing may be different due to the different pin designs used in those studies (no re-entrant features).

A periodic banding is evident in the wake of the tool. This banding is similar in appearance to other cross sectional examinations of the "onion ring" structure of the weld nugget.[25,26] The bands have a spacing of approximately 0.58 mm, which corresponds very closely to the actual 0.56 mm tool advance per revolution. This banding has a different appearance on the two sides of the weld. Well-developed bands extend clearly from the center of the weld to a sharp weld nugget boundary on the advancing side of the weld, while the bands become obscured by what appears to be contrast from individual grains and complex, turbulent strain gradients on the retreating side of the weld.

3.4 Plan View Cross Section Texture and Grain Evolution

Electron backscattered diffraction was used to analyze the grain and texture evolutions occurring around the welding tool. EBSD scans were performed in two different orientations

(see Figure 9). Radial scans were performed at a number of locations around the welding tool to reveal the evolution of material as it approaches the tool. In addition, eight tangential scans were performed around the leading edge of the tool to show how the material next to the tool evolves as it is swept around the tool. Pole figures from these scans are shown in Figure 10. In this figure, the reference frame of the pole figures is rotated with respect to the weld so as to align the horizontal axis with the tangential direction of the tool; this also roughly aligns the presumed shear direction (SD) with the horizontal axis. While five of these scans do not display any apparent systematic textures, there are three regions with similar components of the B fiber shear textures ({hkl}<110>||{shear plane normal}<SD>). Specifically, the 4^{th}, 6^{th}, and 8^{th} scans clockwise from left have a {112}<110> shear component with <111> aligned in the normal direction. In addition, the 1^{st} and 3^{rd} scans show <110>||SD. The B fiber has been reported [27] to be a high temperature shear texture. The periodic decomposition of these textures appears consistent with the initial predictions of texture models of stainless steel friction stir welds [28]. That model predicts that the shear textures developing at the tool break down as they are swept around the tool and transition to new shear texture orientations.

Electron backscattered diffraction was also used to analyze the grain and texture development occurring around the welding tool. The material is swept around from the advancing side to the retreating side ahead of the tool. Towards the advancing side (Figure 11)), the grain refinement does not occur uniformly ahead of the tool, but instead occurs in bands that extend about 1/4 mm ahead of the refined region. The spacing of these bands is about 6 times finer than that of the bands observed in the wake of the tool (which correspond to the tool advance per revolution). This band spacing is therefore unlikely to have been caused by either features on the welding tool or an asymmetry in the welding process. Instead, these bands appear to correspond to a heterogeneity of the grain refinement processes induced by the deformation field surrounding the tool. This may result from variations in the relative susceptibility of different orientations to form subgrains due to their orientation stability with respect to the applied deformation [29] and/or preferential refinement at pre-existing substructure (e.g., continuous dynamic recrystallization by progressive lattice rotation [30]) in the surrounding grains.

The variations in grain evolution are more evident in Figure 12, which is a higher resolution scan from the subregion indicated in Figure 11. This scan reveals the fine structure within two nearly vertical bands of refined grains in addition to other grains with various stages of subgrain development. Both grain and subgrain boundaries are revealed in the image quality map (Figure 12b), which reflects the relative EBSD pattern intensity at each point. These grain boundaries are colored according to their misorientation angle in Figure 12c to show the network of red (<2° misorientation) and blue (2-15º misorientation) low-angle boundaries (LABs) interspersed throughout the structure. The LABs comprise 36% of total boundary length at this location.

The grain refinement ahead of the tool (across Figure 11) appears to evolve continuously throughout whole grains as subgrains gradually develop ever-increasing boundary misorientations. The subgrain size remains essentially constant from the point where they are first observable to the final refined grain structure near the tool. The evolution in grain boundary character is more quantitatively shown in Figure 13, which shows a continuous and gradual increase in misorientation of the lower angle (<25°) boundaries in the direction towards the welding tool. These results demonstrate that there is a continuous evolution of subdivision progression and resultant boundary misorientations in addition to the orientation-dependent heterogeneity of the subdivision processes. Generation of LABs within the larger persistent grains suggests that subdivision by dislocation rearrangement and grain rotation is in the process of refining these grains as well. While there are some instances where refined

grains are observed at the previous high-angle grain boundaries, which would be indicative of dynamic recrystallization due to progressive subgrain rotation, most of the refined grains are not restricted to such locations.

Similar characteristics are present directly in front of the tool along the welding direction (Figure 14). The grain refinement again develops in broad bands ahead of the refined region and the developing subgrains are similar in size to the refined grains. The larger grains between the bands of refined grains exhibit another similarity. Although not discernible in Figures 11 and 14, these unrefined grains are all oriented such that <110> is near to the tool's tangential direction, which is the presumed shear direction. This coincides with the B fiber for fcc shear textures [31]. This indicates that these coarse grains are in a more stable and subdivision-resistant orientation than the surrounding grains, explaining why the grain subdivision process is more advanced in some grains than in others.

The fully refined region adjacent to the tool in Figure 14 has a crystallographic texture similar to that of the refined region of Figure 11, although it is more strongly developed. The form of this texture, shown in Figure 15a, is more evident after aligning the crystal reference frame with the principal axes of the deformation field responsible for the texture evolution, as shown in Figure 15b. The predominant deformation in FSW is expected to be simple shear, which is typically displayed in pole figures with a vertical shear plane-normal (SPN) and a horizontal shear direction (SD). In order to achieve this representation, with the shear plane tangential to the tool and the shear direction along the weld transverse direction (TD), the textures shown in Figure 15a were rotated by 90° about the ND relative to Figure 14. However, an additional 37° rotation counter-clockwise about the TD and 10° rotation clockwise about the ND is necessary to produce the texture shown in Figure 15b, which exhibits the monoclinic sample symmetry associated with simple shear processing. In fact, the rotated texture (Figure 15b) closely resembles that of ideal simple shear textures in fcc metals [32]. These additional required rotations suggest the influence of rigid rotation of material near the stir zone and indicate the complexity of the flow field. Thus, the texture development occurring ahead of the FSW tool appears to result predominantly from a simple shear deformation field. The existence of a shear texture in the refined region ahead of the weld, together with the observations of substructure development discussed above, suggests that the grain refinement occurring ahead of the tool is primarily caused by plastic spin and rigid rotations associated with shear deformation processes [33], rather than by dynamic recrystallization [30]. Attendant dynamic recovery processes would also affect the substructural evolution.

As the material is swept around the front of the tool, the texture evolves from the simple shear texture shown in Figure 15. By the time the material has been transported 90° from the welding direction, the refined structure exhibits a texture (Figure 16) with pronounced strengthening of <111>||ND, and the development of two components within the <111> fiber. These components represent the condensation of the fcc shear texture into two of its constituents, referred to in the literature as the B and $\overline{B}$ shear orientations [34]. The relationship of this texture to that of the typical shear texture ahead of the weld (Fig. 15b) is readily apparent. Individual shear texture components typically evolve in strength with increasing strain [35], so the texture modification may be due to accumulation of greater total strain on the retreating side of the weld. Continuous dynamic recrystallization or recovery subsequent to the initial grain refinement could also change the initial texture. This <111>||ND texture can also be observed in the nugget of the deposited weld [36] and is similar to textures observed in the weld nuggets of friction stir welds in 2024 Al [20] and 1100 Al [14].

In the wake of the tool (Figure 17), the crystallographic texture exhibits a periodic banding similar to that observed by optical microscopy (Figure 8). The band spacing again

corresponds to the advance per revolution of the welding tool. The material adjacent to the tool was entrained in the flat of the tool, and was therefore not analyzed. The periodic blue-colored bands exhibit a {112}<110> shear component which is very sharp for the first band then becomes less distinct for the subsequent bands. The initial orange-colored band exhibits a slightly rotated shear texture similar to that observed in front of the tool (Figure 15). The next band exhibits a texture which appears to be transitional between the shear texture observed in the first band and the {112}<110> texture. Subsequent bands exhibit one or the other of the two constituent shear orientations (B and $\overline{B}$) of the {112}<110> texture. This texture evolution through the first few textural bands is in agreement with the color change associated with the first few orange/green bands, indicating that the texture continues to evolve after its initial deposition for more than 1 mm in the wake of the weld.

4.0 Summary

Two orthogonal views of a friction stir weld were analyzed to determine the microstructure, crystallographic texture, and grain structure of the deposited weld and how these characteristics initially developed in the vicinity of the weld tool.

The transverse cross section reveals many interesting features. There is a complex precipitation sequence across the different weld regions. The strengthening precipitates from the matrix become coarsened across the HAZ, then are gradually replaced by a separate precipitate distribution, which forms during cooling of the weld, in the TMAZ. A third precipitate distribution that includes the equilibrium T_B phase is observed in the weld nugget and is responsible for the lower microhardness of that region. A coarsening of grains is observed in the TMAZ adjacent to the weld nugget, accompanied by an in-plane rotation of the grains towards <110>||welding direction. The latter observation suggests that this texture evolution is primarily in response to a simple-shear deformation field surrounding the tool.

A plan-view section through the embedded FSW tool of this stop-action weld was prepared to reveal the initial development and evolution of the grain structure and crystallographic texture during friction stir welding. This analysis revealed bands of refined grains developing ahead of the fully refined region, likely reflecting different relative stabilities of the original grain orientations to the applied deformation. The initial development of the refined grain structure appears to occur by formation of fine subgrains induced by simple-shear deformation. These subgrains gradually develop greater misorientations with increased strain. The refined grains adjacent to the tool display a typical fcc shear texture after suitable rigid rotations are applied. As the material is swept around the welding tool, the texture of the refined grains evolves from the fcc shear texture to a modified texture principally consisting of two <111>||ND shear components. The primary mechanism of grain refinement in this weld therefore appears to be subdivision induced by deformation and dynamic recovery processes, with the possibility, but not necessity, of a concurrent dynamic recrystallization mechanism.

5.0 Acknowledgements

The authors gratefully acknowledge support for this research through the ONR Industrial Programs office (RWF) and through the U.S. Department of Energy under Contract W-7405-Eng-36 (JFB).

6.0 References

1. W.M. Thomas, E.D. Nicholas, J.C. Needham, M.G. Murch, P. Templesmith, and C.J. Dawes, "Friction Stir Butt Welding", Int. Patent App. PCT/GB92/02203 and GB Patent App. 9125978.8, Dec. 1991. U.S. Patent No. 5,460,317, Oct. 1995.
2. K.J. Colligan, Proc. 1st Int. Sym. on Friction Stir Welding, TWI, Cambridge (1999).
3. A.P. Reynolds, T.U. Seidel, and M. Simonsen, Proc. 1st Int. Sym. on Friction Stir Welding, TWI, Cambridge (1999).
4. K.J. Colligan, *Welding Journal*, **78** (7), 229s-237s (1999).
5. T.U. Seidel and A.P. Reynolds, *Met Mat Trans A*, **32A**, 2879-2884 (2001).
6. B. London, M. Mahoney, W. Bingle, M. Calabrese, and D. Waldron, Proc. 3rd Int. Sym. on Friction Stir Welding, TWI, Cambridge (2001).
7. J.H. Ouyang, D. Jandric, R. Kovacevic, M. Song, and M. Valant, Proc. 6th Int. Conf. on Trends in Welding Research, ASM International, Materials Park, OH, pp. 229-234 (2003).
8. J.C. McClure, E. Coronado, S. Aloor, B.M. Nowak, L.E. Murr, and A.C. Nunes, Jr., Proc. 6th Int. Conf. on Trends in Welding Research, ASM International, Materials Park, OH, pp. 257-261 (2003).
9. T. Dickerson, H.R. Shercliff, and H. Schmidt, Proc. 4rth Int. Sym. on Friction Stir Welding, TWI, Cambridge (2003).
10. B. London, M. Mahoney, W. Bingel, M. Calabrese, R.H. Bossi, and D. Waldron, Friction Stir Welding and Processing II, TMS, Warrendale, PA, pp. 3-12 (2003).
11. Y. Li, L.E. Murr, and J.C. McClure, *Mat Sci Eng A*, **271**, 2213-223 (1999).
12. H. Jin, S. Saimoto, M. Ball, and P.L. Threadgill, *Mat Sci Tech*, **17**, 1605-1614 (2001).
13. Y.S. Sato, H. Kokawa, K. Ikeda, M. Enomoto, S. Jogan, and T. Hashimoto, *Met Mat Trans A*, **32**, 941-948 (2001).
14. D.P. Field, T.W. Nelson, Y. Hovanski, and K.V. Jata, *Met Mat Trans A*, **32**, 2869-2877 (2001).
15. K.V. Jata and S.L. Semiatin, *Scripta Mat*, **43**, 743-749 (2000).
16. A.F. Norman, I. Brough, and P.B. Prangnell, *Mat Sci Forum*, **331-337**, 1713-1718 (2000).
17. D.P. Field and T.W. Nelson, *Mat Sci Forum*, **408-412**, 1507-1512 (2002).
18. Y. Hovanski, T.W. Nelson, and D.P. Field, *Proc Joining of Advanced and Specialty Metals*, ASM Intl., Materials Park, OH, 167-171 (2001).
19. J.-Q. Su, T.W. Nelson, R. Mishra, and M. Mahoney, *Acta Mater*, **51**, 713-729 (2003).
20. M. Karlsen, Ø. Frigaard, J. Hjelen, Ø. Grong, and H. Norum, *Mat Sci Forum* **426-432**, 2861-2866 (2003).
21. Y.S. Sato, H. Kokawa, M. Enomoto, and S. Jogan, *Met Mat Trans A*, **30A**, 2429-2437 (1999).
22. K.V. Jata, K.K. Sankaran, and J.J. Ruschau, *Met Mar Trans A*, **31A**, 2181-2192 (2000).
23. Ø. Frigaard, Ø. Grong, and O.T. Midling, *Met Mat Trans A*, **32A**, 1189-1200 (2001).
24. R.W. Fonda and J.F. Bingert: *Met Mat Trans A*, 35A, 1487-1499 (2004).
25. M.A. Sutton, B. Yang, A.P. Reynolds, and R. Taylor, *Mat Sci Eng A*, **323**, 160-166 (2002).
26. K.N. Krishnan, *Mat Sci Eng A*, **327**, 246-251 (2002).
27. F. Montheillet, M. Cohen, and J.J. Jonas, *Acta Metall*, **32**, 2077-2089 (1984).
28. P.R. Dawson, presentation at ONR Friction Stir Welding Workshop, Flintstone, MD May 10-13, 2004.
29. Q. Liu, D. Juul Jensen, and N. Hansen, *Acta mater.*, **46**, 5819-5838 (1998).
30. F.J. Humphreys and M. Hatherly, Recrystallization and Related Annealing Phenomena, Elsevier Science, Oxford, 1995, pp. 145-146 & 369-382.
31. F.J. Humphreys and M. Hatherly, *op. cit.*, pp. 380-381.

32. G.R. Canova, U.F. Kocks, and J.J. Jonas, *Acta Metall.*, **32**, 211-226 (1984).
33. M.R. Barnett and F. Montheillet, *Acta mater.*, **50**, 2285-2296 (2002).
34. L.S. Tóth, K.W. Neale, and J.J. Jonas, *Acta Metall.*, **37**, 2197-2210 (1989).
35. F. Montheillet, P. Gilormini, and J.J. Jonas, *Acta Metall.*, **33**, 705-717 (1985).

Figures

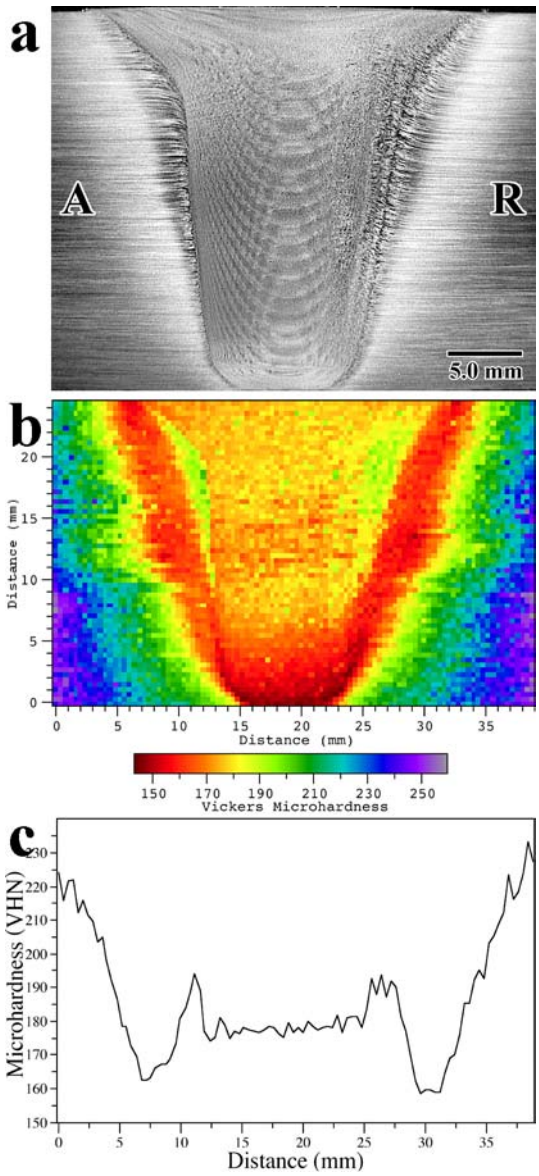

Figure 1. (a) Optical macrograph of weld transverse cross section, (b) corresponding microhardness map, and (c) microhardness linescan 20 mm above base of weld

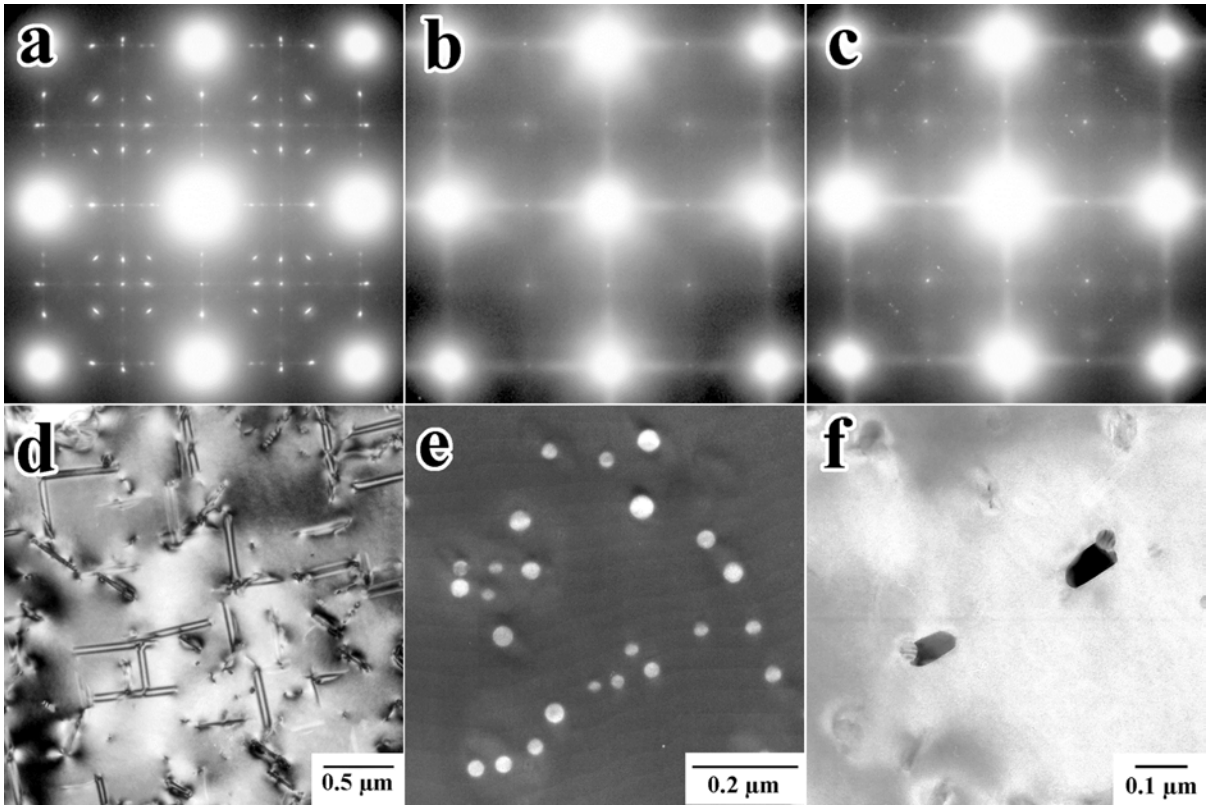

Figure 2. Electron diffraction patterns and transmission electron micrographs from (a,d) the HAZ region, (b,e) the TMAZ region, and (c,f) the weld nugget.

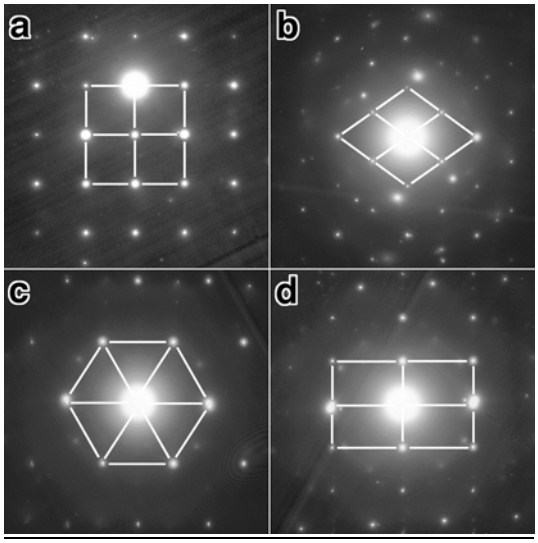

Figure 3. Electron diffraction patterns from the (a) 100, (b) 110, (c) 111, and (d) 112 zone axes of the rod-shaped precipitates in the weld nugget region.

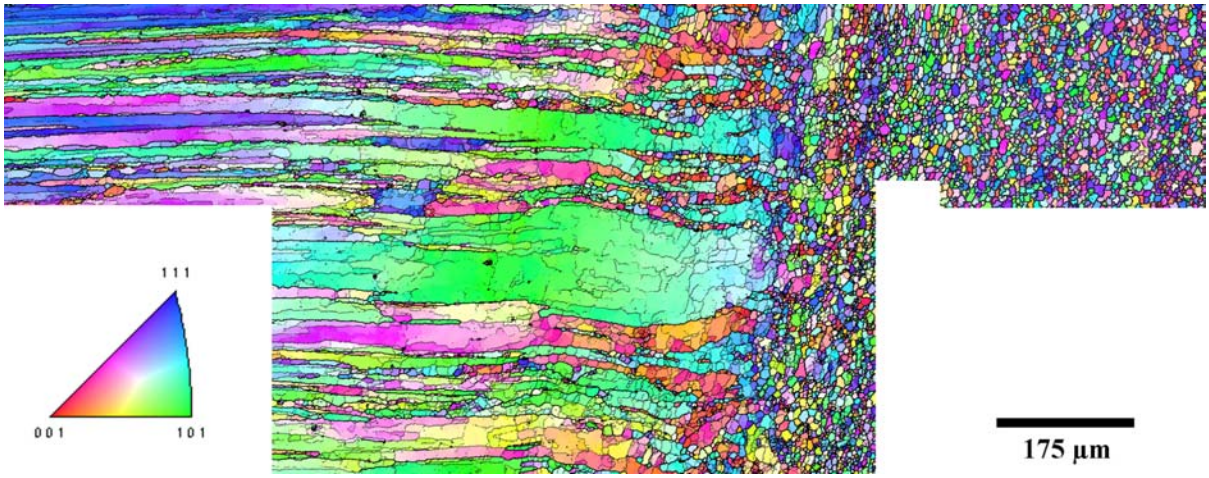

Figure 4. Crystal direction map across the advancing side weld nugget boundary, with stereographic triangle showing the direction of grains with respect to the viewing (welding) direction.

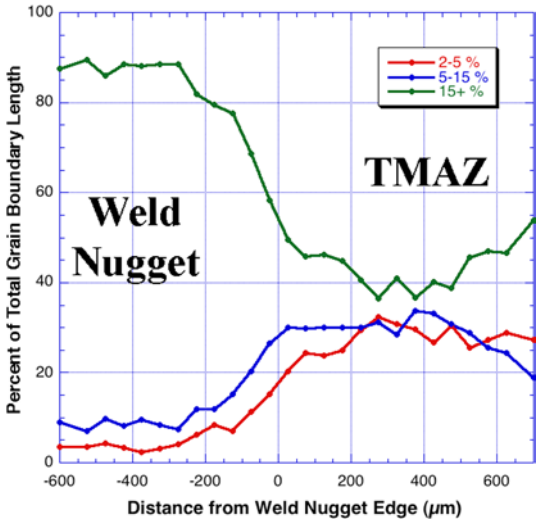

Figure 5. Graph of grain boundary misorientation across region shown in Figure 4.

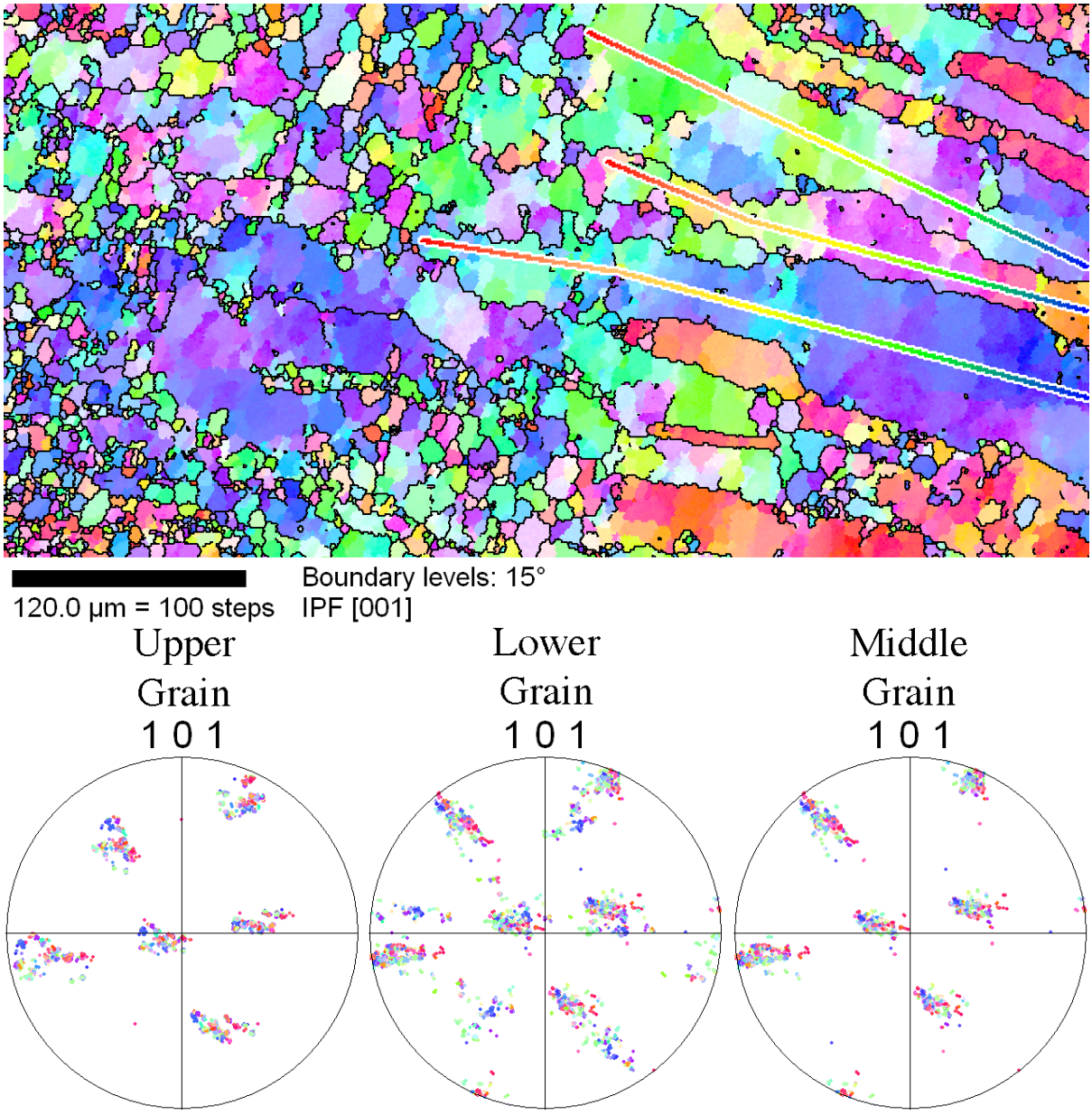

Figure 6. (a) (top) Crystal direction map across the retreating side weld nugget boundary and (b) (bottom) pole figures of the grain orientation evolutions occurring across the indicated grains. Each orientation is colored according to its location along the corresponding line, with the orientations evolving from blue to red towards the weld center.

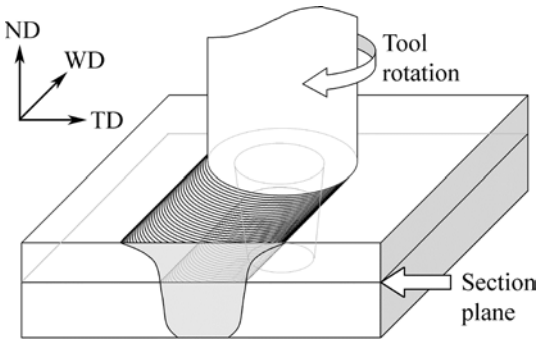

Figure 7. Schematic of the stop-action friction stir weld examined in this study, showing the embedded tool and the location of the plan view surfaces analyzed. The plate normal direction (ND), welding direction (WD) and transverse direction (TD) are indicated.

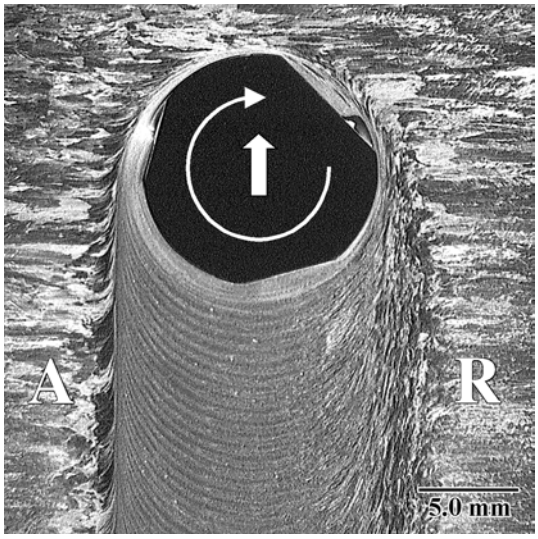

Figure 8. Plan view optical macrograph of the stop-action friction stir weld showing the rotational and translational directions of the tool and the grain development around the embedded tool. Advancing (A) and retreating (R) sides of the weld are labeled.

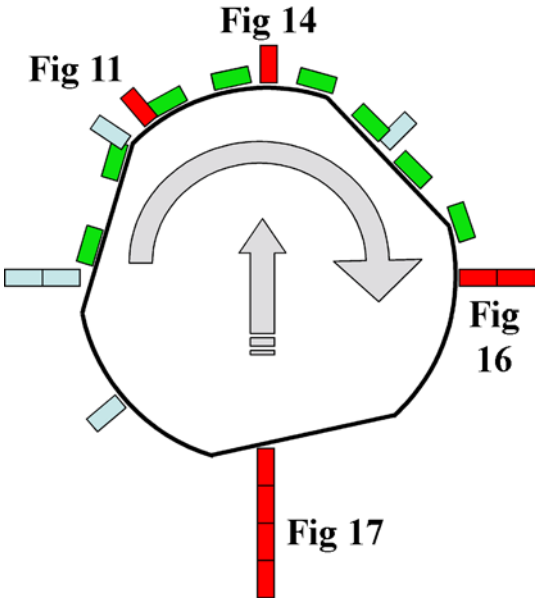

Figure 9. Schematic of the EBSD scans performed on the plan view specimen, with the tangential scans shaded green. The red-shaded radial scans are labeled with their corresponding figure numbers.

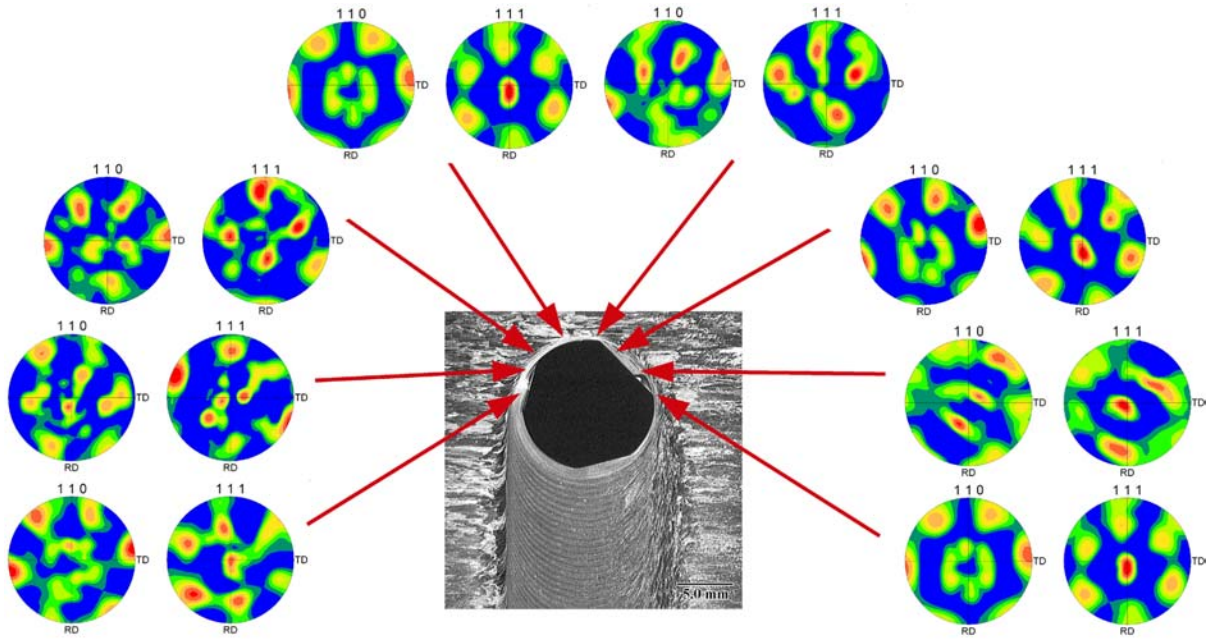

Figure 10. Pole figures from the tangential EBSD scans around the front of the welding tool. Sample reference frame of the pole figures rotates to align the tangential direction of the tool with the horizontal direction of the pole figure.

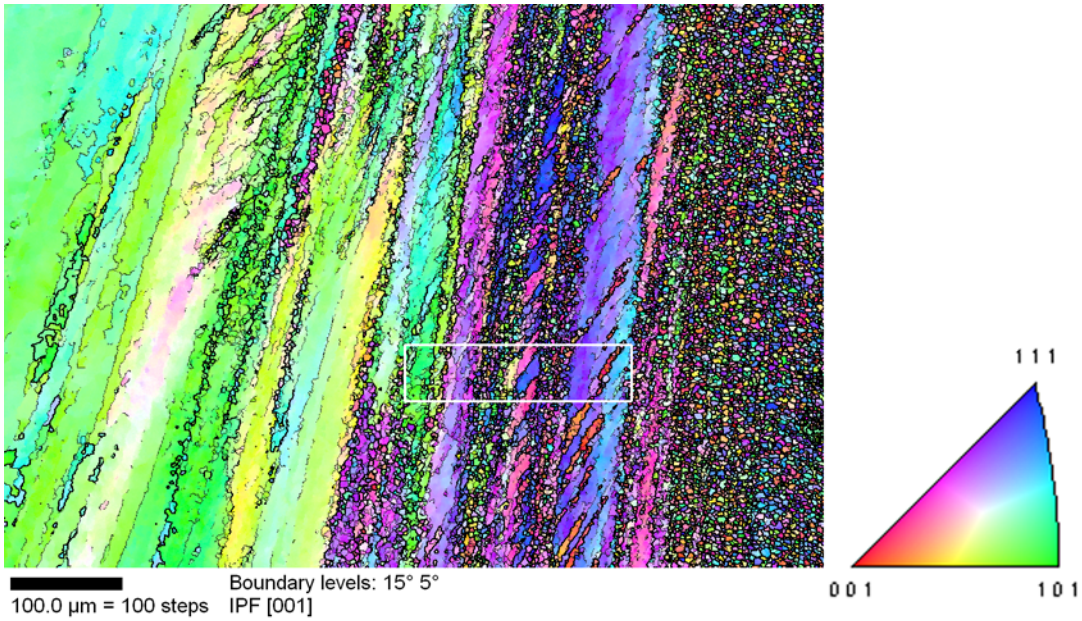

Figure 11. EBSD crystal direction map showing the grain evolution ahead of the tool on the advancing side. Colors represent crystal directions in the viewing direction (along the weld direction). Tool is to the right of this image. Location of this region is indicated in Figure 9, and the white rectangle demarcates region of higher resolution scan shown in Fig. 12.

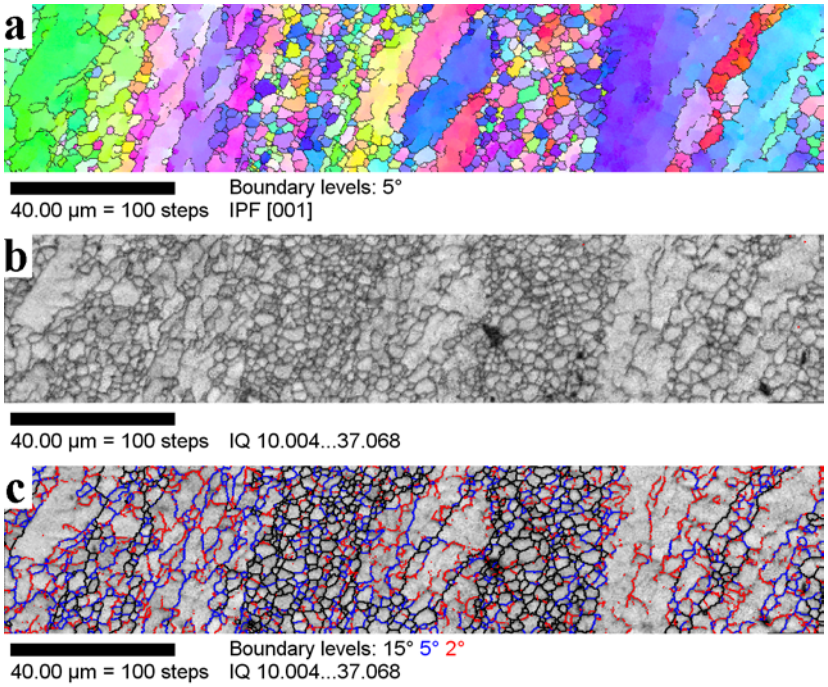

Figure 12. Higher resolution EBSD crystal direction map (a), associated image quality map (b), and image quality map with misorientations demarcated (c) (> 15º black, 5-15º blue, and 2-5º red) from the indicated region shown in Figure 11.

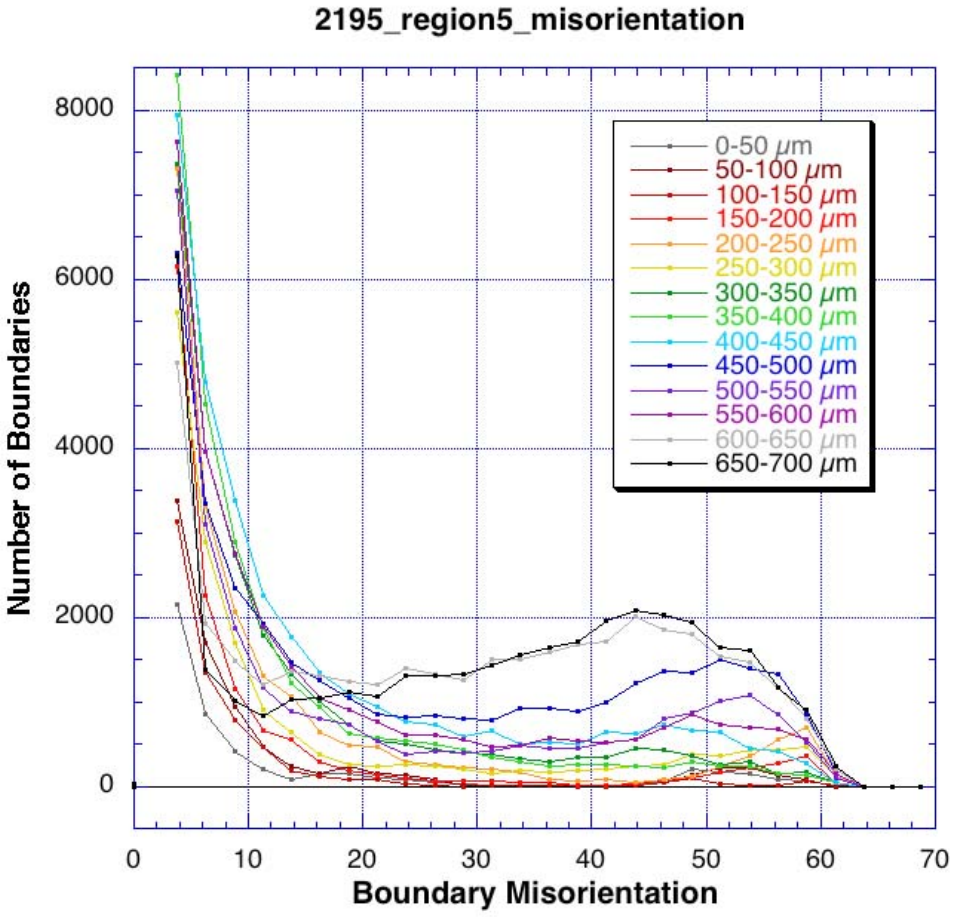

Figure 13. Graph of the grain boundary misorientation as a function of distance from left to right across Figure 11.

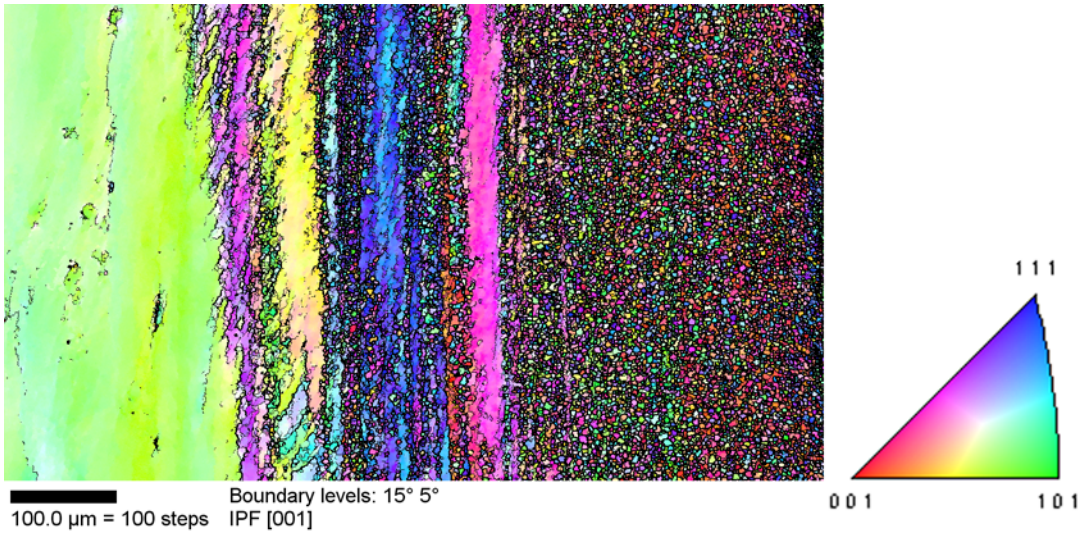

Figure 14. EBSD crystal direction map showing the grain evolution in the welding direction ahead of the tool. Tool is to the right of this image. Location of scanned region is indicated in Figure 9.

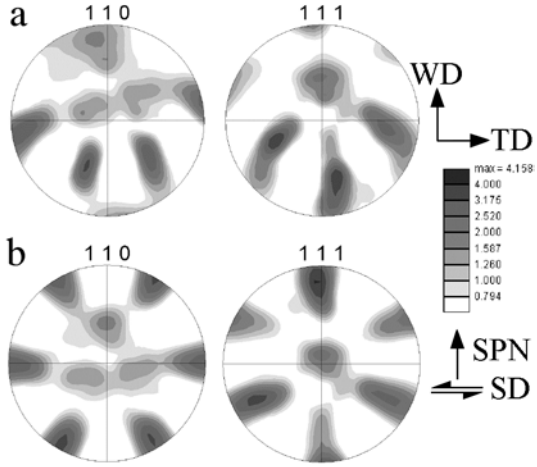

Figure 15. (a) Unrotated and (b) rotated pole figures from the refined grain region in Figure 14. SPN refers to the implied shear-plane normal, and SD the shear direction.

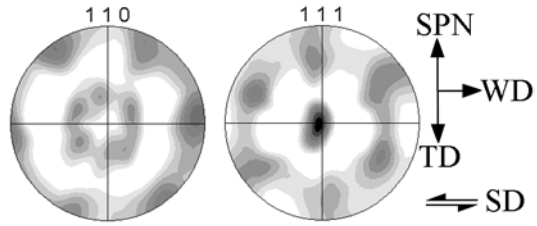

Figure 16. Pole figures from the refined grain region normal to the welding direction on the retreating side of the weld (see Figure 9 for location). SPN refers to the implied shear-plane normal, and SD the shear direction. Scale is shown in Figure 15.

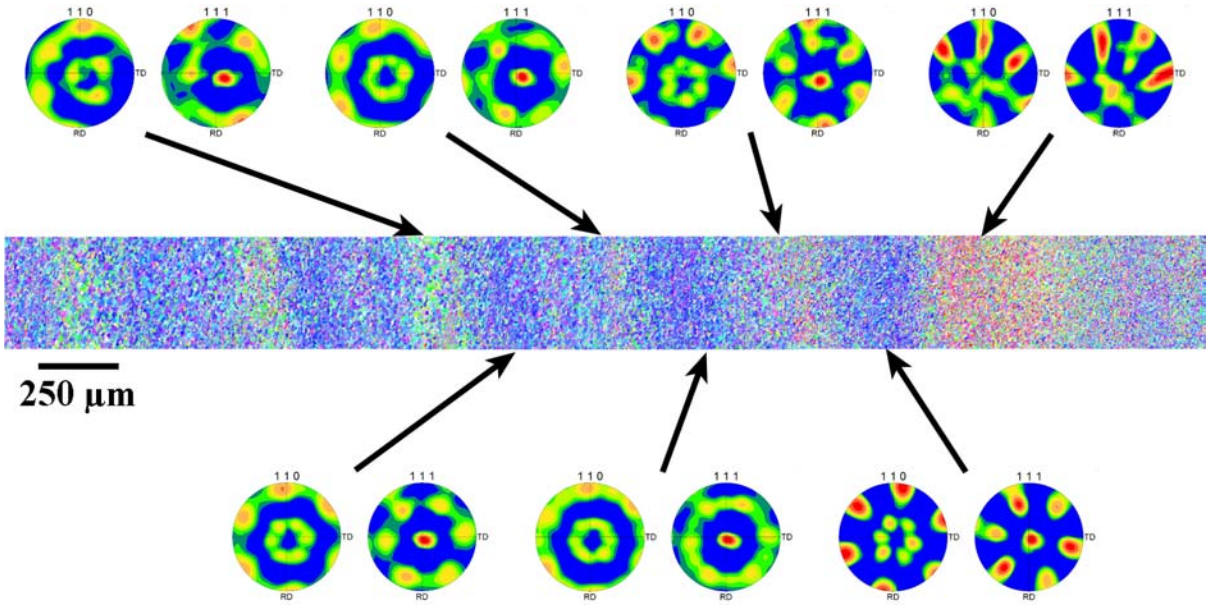

Figure 17. EBSD crystal direction map showing the texture evolution in the wake of the tool. Tool is to the right in this image. Location of scanned region is indicated in Figure 9.